Journal of the Mechanics and Physics of Solids 114 (2018) 97–116

Contents lists available at ScienceDirect

Journal of the Mechanics and Physics of Solids

journal homepage: www.elsevier.com/locate/jmps

Prediction of shock initiation thresholds and ignition probability of polymer-bonded explosives using mesoscale simulations

Seokpum Kim[a,b,1], Yaochi Wei[a,1], Yasuyuki Horie[c], Min Zhou[a,*]

[a] The George W. Woodruff School of Mechanical Engineering, School of Materials Science and Engineering, Georgia Institute of Technology, Atlanta, GA 30332-0405, USA
[b] Oak Ridge National Laboratory, Oak Ridge, TN 37830, USA
[c] (ret.) Air Force Research Lab, Munitions Directorate, 2306 Perimeter Road, Eglin AFB, FL 32542, USA

ARTICLE INFO

Article history:
Received 26 June 2017
Revised 19 February 2018
Accepted 20 February 2018
Available online 21 February 2018

Keywords:
PBX
Energetic material
Ignition threshold
Binder properties
Energy dissipation

ABSTRACT

The design of new materials requires establishment of macroscopic measures of material performance as functions of microstructure. Traditionally, this process has been an empirical endeavor. An approach to computationally predict the probabilistic ignition thresholds of polymer-bonded explosives (PBXs) using mesoscale simulations is developed. The simulations explicitly account for microstructure, constituent properties, and interfacial responses and capture processes responsible for the development of hotspots and damage. The specific mechanisms tracked include viscoelasticity, viscoplasticity, fracture, post-fracture contact, frictional heating, and heat conduction. The probabilistic analysis uses sets of statistically similar microstructure samples to directly mimic relevant experiments for quantification of statistical variations of material behavior due to inherent material heterogeneities. The particular thresholds and ignition probabilities predicted are expressed in James type and Walker–Wasley type relations, leading to the establishment of explicit analytical expressions for the ignition probability as function of loading. Specifically, the ignition thresholds corresponding to any given level of ignition probability and ignition probability maps are predicted for PBX 9404 for the loading regime of $U_p = 200$–1200 m/s where U_p is the particle speed. The predicted results are in good agreement with available experimental measurements. A parametric study also shows that binder properties can significantly affect the macroscopic ignition behavior of PBXs. The capability to computationally predict the macroscopic engineering material response relations out of material microstructures and basic constituent and interfacial properties lends itself to the design of new materials as well as the analysis of existing materials.

1. Introduction

Energetic materials (EM) have a wide range of applications such as propellants, fuels, explosives, automobile air bags and pyrotechnics. Technical challenges for the design of EM include optimization with minimal trade-off among (1) performance

* Corresponding author. Also with Sichuan University and Chengdu University, China.
E-mail address: min.zhou@gatech.edu (M. Zhou).
[1] These two authors contributed equally to this paper.

https://doi.org/10.1016/j.jmps.2018.02.010
0022-5096/

– how to increase the energy content of EM and the delivery of power; (2) reliability – how to accurately control intended detonation and avoid accidental detonation; and (3) how to ensure the survivability and integrity of EM against mechanical (e.g., impact, accidental loading) insults. Solutions to these challenges largely depend on the design of the materials' microstructures. However, changes in a microstructure in general affect all three attributes simultaneously rather than individually. As a result, trade-offs may have to be accepted in the development of the materials. Polymer-bonded explosives (PBXs) which consist of energetic particles bonded with a polymer binder have highly heterogeneous microstructures, thus the analysis of the effect of microstructure is important and intrinsically challenging. The design of PBXs with considerations of the trade-offs to date has relied on empiricism and intuition based on numerous trial-and-error interactions. For example, increasing the binder content may help improve the survivability, but leads to lower energy content in the overall material. In order to develop the next-generation energetic materials, a paradigm-shifting approach is required which transforms the development of EM from the historical empiricism to modeling and simulation based design science that accounts for microstructural characteristics and processing. The simulations should also address the stochastic nature of the ignition of EM due to the heterogeneous nature of the materials. The microstructure scale or meso scale for PBXs concerns material heterogeneities on the order of microns (μm) to hundreds of microns. It is at this scale that materials processing and synthesis have one of the most significant influences on material structural hierarchy – for a given combination of constituents and composition of a material. Naturally, this scale is one of the focuses of PBX design, both experimentally and computationally.

Since microstructural heterogeneities greatly affect hotspot formation which is the mechanism determining the ignition of EM, there have been several attempts to directly model the heterogeneities of energetic materials. To understand the effect of pores, Levesque et al. (2013) studied the critical hotspot temperature using the Frank-Kamenetskii analysis (Frank-Kamenetskii, 1969) and obtained critical pore sizes in HMX subject to loading with various shock pressures. To understand the effect of microstructural morphology on hotspot formation, Baer (2002) analyzed the response of PBXs under shock loading. The hotspots obtained in his study are from thermo-mechanical energy dissipation without reaction. To obtain the detonation response, he performed ignition/growth reactive burn calculations separately from the hotspot formation calculations. Significant fluctuations are observed in the shock wave and the detonation wave, indicating that the waves do not move the material state to a single jump state in a heterogeneous material. Under low intensity loading ($U_p = 280$ m/s) where U_p is the particle velocity, calculations with an Eulerian approach (Menikoff, 2002) on a granular HMX pack showed that the maximum hotspot temperature is low ($T_{max} < 450$ K). Under moderate intensity loading ($300\,\text{m/s} < U_p < 500\,\text{m/s}$), calculations with a Lagrangian approach (Gilbert et al., 2013) showed significant numbers of hotspots with higher temperatures ($T > 500$ K) in a granular HMX pack. The hotspots in their Lagrangian calculations are generated by frictional dissipation at the boundaries of grains without intragranular fractures and plastic deformation. It is computationally challenging to analyze the entire detonation process all the way from local ignition, while both the hotspot formation events and microstructure morphology are explicitly resolved. Recently, Rai and Udaykumar (2015) used an Eulerian finite element method (FEM) coupled with a multi-step chemical kinetics model to predict the initiation of pressed HMX with microstructures of specimens in the experiments of Welle et al. (2014a). The study focused on hotspot evolution through chemical reaction and showed local initiation in one of the samples. However, there has been little study on the microstructural effect of multi-constituent PBX on the initiation under a wide range of load intensity, from low velocities ($U_p < 300$ m/s) to the shock regime ($U_p > 1$ km/s).

Historically, the determination of shock initiation thresholds for the purpose of explosives engineering has relied exclusively on experimental observations of "go" and "no go" events under a given loading condition (i.e., a combination of load intensity and loading time). The thresholds are fitted to analytical forms involving parameters of loading conditions such as load intensity in the form of shock pressure, projectile velocity, or particle velocity in a specimen and loading time in the form of load duration or flyer thickness. For instance, the shock-wave initiation threshold proposed by Walker and Wasley (1969) is based on shock pressure and load duration. James (1996) later developed a threshold relation in terms of the kinetic energy of the flyer and the total energy input. Other analytical forms of initiation threshold are listed in Solov'ev (2000).

In this paper, we present a numerical framework for predicting the ignition event and, through which, the ignition threshold of PBXs. The configuration of analysis involves thin-pulse shock-wave loading, which is a computational representation of thin-flyer shock experiments (Welle et al., 2014b; Swift et al., 2005). The computational model explicitly considers microstructure effects including random morphology of constituents, energetic particle size distribution, binder properties, and particle-binder interface response. The framework and computational capability result from our recent efforts (Barua et al., 2013a,b; Barua and Zhou, 2011; Kim et al., 2014,2016) which are based on a Lagrangian cohesive finite element method that explicitly track essential mechanical and thermal processes. The framework of analysis is based on an assumption that the attainment of criticality by hotspots for self-sustained thermal explosion correlates (or is equivalent) to the ignition threshold for initiating detonation, which is supported by James and Lambourn's observation (James and Lambourn, 2006). Specifically, James and Lambourn found that reaction behind shock wave fronts is a function of shock strength and time along the particle path and is independent of local flow variables (such as pressure and temperature) behind the shock. Therefore, growth in the pressure or temperature fields does not feed back to the reaction rate. This observation suggests that there is a one-to-one correspondence between the existence of critical hotspots which lead to local thermal runaway and the occurrence of eventual detonation. The attainment of critical hotspots indicates the point where chemistry can be self-sustaining. Therefore, from this point, chemical reaction can take over and lead to subsequent burn and eventual outcome of detonation. In this paper, we do not consider the issue of subsequent burn after hotspots reaching a critical state

and the time needed to reach detonation. Rather, we are solely concerned with the determination of the ignition threshold via hotspot criticality. The criticality of hotspots in samples is ascertained through an ignition criterion developed recently (Barua et al., 2013a). Details of the hotspot ignition criterion are discussed in Section 2.4.

This paper consists of two parts. The first part describes the computational framework and the materials analyzed. PBX 9404 is chosen because it is HMX-based explosive composites with similar HMX fractions and often chosen for comparison (Mulford and Swift, 2002). The second part discusses the predicted initiation thresholds and compares the prediction with available experimental data. A particular emphasis is placed on quantifying the probabilistic nature of the ignition thresholds resulting from intrinsic material heterogeneities. For this purpose, sets of multiple samples with statistically similar microstructures are generated and used in direct mimicking of experimental quantification of statistical distributions of material behavior.

2. Framework of analysis

2.1. Materials and microstructures

Polymer-bonded explosives (PBXs) are heterogeneous composites consisting of energetic particles and a polymer binder. The energetic particles in practical use include HMX, RDX, TATB, and PETN. Among these, HMX (Octahydro-1,3,5,7-tetranitro-1,3,5,7-tetrazocine) holds the highest energy density, therefore, has drawn intense interest for several decades (Christiansen and Taylor, 1973; Hayes, 1976; Bennett et al., 1998; Austin et al., 2015). HMX-based PBXs include PBX 9404, which consists of HMX (94wt.%), Nitrocellulose (NC) (3wt.%), and a plasticizer (3wt.%).

In this study, the microstructures that are computationally generated have an HMX grain volume fraction of 81% and a binder volume fraction of 19%. The theoretical volume fraction of HMX in PBX 9404 is 91.5%. However, lower HMX volume fractions are typically observed in actual microstructures because some HMX particles are too small to be resolved and some are absorbed in the binder. For example, Benson and Conley (1999) observed a binder volume fraction of 26% from a micrograph of PBX 9501 whose theoretical volume fraction of a binder is only around 8%. Mas et al. (2006) observed a binder volume fraction of 23% for PBX 9501 and reproduced the stress-strain behavior using an explicit finite element framework. Barua and Zhou (2011) used the microstructures of PBX 9501 with an HMX volume fraction of 82% in their numerical study and obtained stress-strain curves that match experimental data. This paper uses the same HMX volume fraction for PBX microstructures and the same numerical framework (cohesive finite element method) as those used by Barua and Zhou (2011).

The HMX particles in PBX microstructures typically have random polygonal shapes (Benson and Conley, 1999; Dattelbaum and Stevens, 2008; Liu, 2003). To obtain computational PBX microstructures similar to those of experimental specimens, a library of HMX grains extracted from microstructures generated by Voronoi tessellation is first established, with the sizes of the grains systematically tabulated. The grains are then used to compose PBX microstructures with prescribed grain volume fractions and grain size distributions. Details of the method used to generate the microstructures and the attributes of the microstructures are described in Kim et al. (2014). This approach allows large numbers of microstructure samples with prescribed grain size distributions and other attributes to be obtained efficiently. In this section and the following discussions, we use the term “samples” to indicate computationally generated microstructures for finite element simulations and “specimens” to indicate experimentally used ones. Sets of multiple samples (five for each set) with statistically equivalent attributes but different random distributions of the constituents are generated and used. Computationally analyzing the behavior of a set of multiple statistically similar samples is equivalent to carrying out experiments on multiple specimens of the same material, both allowing the statistical variations and probabilistic distributions of material behavior to be quantified. To illustrate the random variations in microstructure morphology and the statistical consistency among multiple samples, Fig. 1 shows five samples with the same HMX volume fraction of $\eta = 0.81$ and the variations in grain size distributions among the samples. The grains have an average size of 210 μm and a monomodal size distribution with a standard deviation of 66 μm.

2.2. Loading configuration

The computational model emulates the experiments with a thin-flyer launched by an electric gun (E-gun) impacting on a PBX specimen as carried out by Weingart et al. (1980). The impact generates a loading pulse which propagates through the specimen, as seen in Fig. 2 of Springer et al. (2014). The boundary conditions and the loading conditions imitate the condition of such experiments. Specifically, impact loading is effected by applying a prescribed particle velocity at the impact face (left boundary of the sample) for a specified time duration, as shown in Fig. 2. The top and bottom boundaries are constrained such that lateral expansion does not occur. This is a 2D model and the conditions of plane-strain prevail. This configuration approximates the planar shock pulse loading of a sample under conditions of approximate macroscopic uniaxial strain. The imposed particle velocity and duration are chosen to correspond to the loading characteristics in the shock experiments (Weingart et al., 1980), in which flyer velocities range from 1–5 km/s, and the flyer thickness varies from 1.27 mm to 25 μm. The imposed particle velocity depends on the impedances (ρU_s) of the flyer and the PBX sample. The range of loading conditions analyzed in the experiment corresponds to the imposed particle velocity range of $U_p = 371$–1960 m/s. In the calculations, the range of $U_p = 200$–1200 m/s is considered. The pulse duration is determined by the flyer

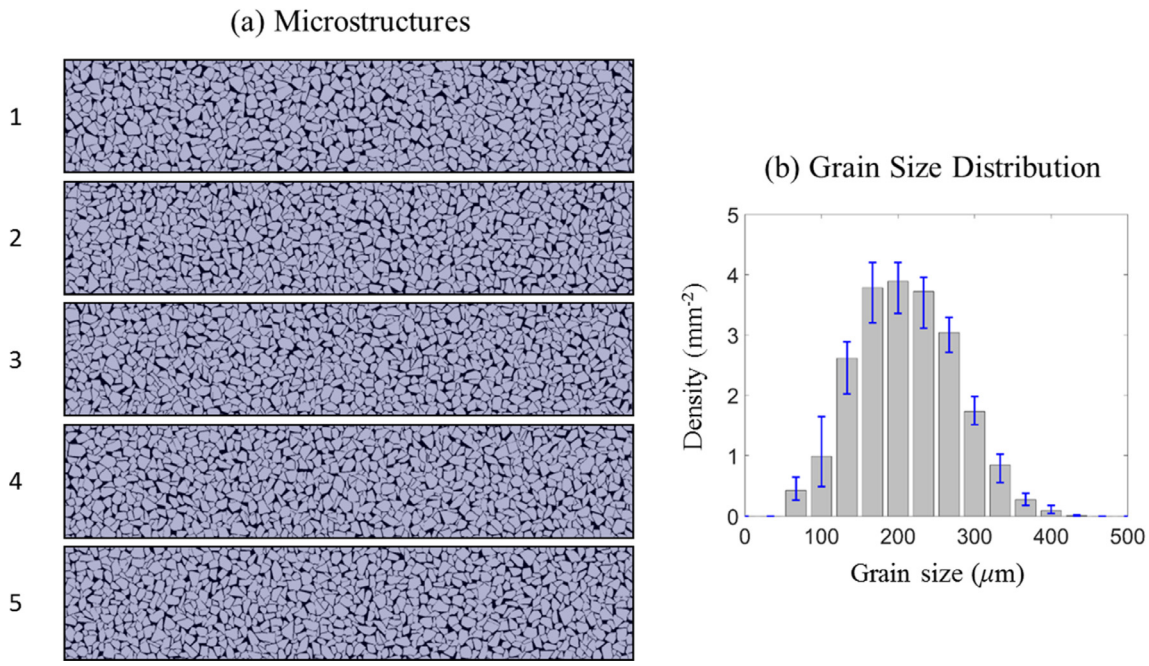

Fig. 1. Computationally generated statistically similar microstructures with a grain volume fraction of $\eta = 0.81$ (a) images of multiple instantiations and (b) HMX grain size distribution.

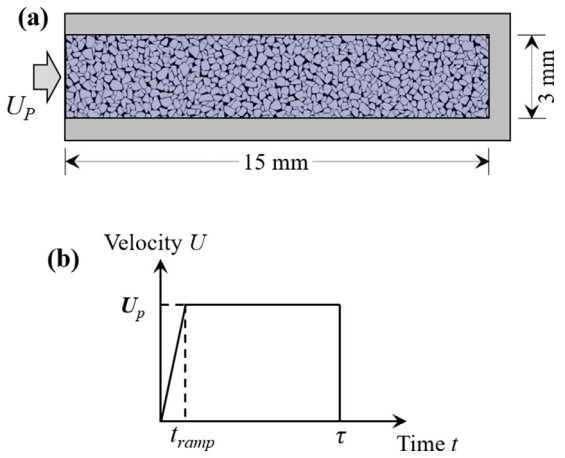

Fig. 2. (a) Configuration of computational model for shock experiments, loading, and boundary conditions considered, and (b) load history imposed on the left boundary of the domain.

thickness, and it is equivalent to the time it takes the longitudinal wave to traverse a round trip in the flyer. The range of flyer thickness in the experiment (Weingart et al., 1980) corresponds to a pulse duration range of $\tau = 8$–980 ns. The pulse durations used in this study range from 20 ns to 4.5 μs. To precisely determine the threshold (load) pulse duration for ignition at each load intensity (imposed particle velocity at impact face, denoted as U_p), multiple simulations are carried out for each sample with loading of successively longer durations. For example, for a given load intensity of $U_p = 200$ m/s, the load duration of $t_{pulse} = 1.5$ μs is used for all microstructures. Then, with the same load intensity, a slightly increased load duration is imposed on all microstructures. This process is repeated until the load duration reaches $t_{pulse} = 4.55$ μs with the minimum increment of $\Delta t_{pulse} = 50$ ns. This procedure is performed for all load intensities ($U_p = 200$–1200 m/s). The load durations and the increments between load durations are dependent on the load intensity, since higher load intensities require shorter load durations and finer increments between the load durations. The loading conditions used in this study are listed in Table 1, including the imposed velocity, the range of pulse durations, and the minimum increment between successive durations. The profile of the imposed load pulse at the impact face is shown in Fig. 2(b). The velocity increases rapidly from zero to U_p over the ramp time of $t_{ramp} = 10$ ns. This velocity is kept constant until the end of the pulse duration τ. After the pulse ends ($t \geq \tau$), the impact face (left boundary) is released and no external loading is applied, while

Table 1
Load conditions and load increments analyzed.

U_p (m/s)	200	400	600	800	1000	1200
Range of pulse duration t_{pulse}(ns)	1500–4550	200–1200	50–300	30–180	30–80	20–60
Range of E (kJ/cm^2)	0.0350–0.106	0.0196–0.123	0.0100–0.0731	0.00917–0.0819	0.0400–0.0482	0.0327–0.0453
Minimum t_{pulse} interval (ns)	50	30	10	5	2	2

the boundaries on the top, bottom, and right remain constrained in their normal directions. For each velocity and sample, 10 different pulse durations are considered, yielding 300 microstructure-loading combinations (6 velocities × 10 pulse durations × 5 microstructures).

2.3. Constitutive relations

The numerical approach used explicitly captures hotspot evolution due to thermo-mechanical energy dissipation inside PBX microstructures under shock pulse loading. The simulations are performed using a recently developed Lagrangian cohesive finite element (CFEM) framework (Barua et al., 2013a,b; Barua and Zhou, 2011). This framework allows quantification of the effects of microstructure and thermo-mechanical processes, including bulk deformation, interfacial debonding, fracture of grains, and subsequent frictional heating. The constitutive relations for the grains are those of a hydrostatic stress-dependent, elasto-viscoplastic material. The binder follows an elastic-viscoelastic constitutive law. Arbitrary fracture patterns along grain-grain and grain-binder boundaries and inside individual constituents are explicitly captured by the use of cohesive elements embedded throughout the microstructure, along all element boundaries. The cohesive elements follow a bilinear traction-separation law which consists of an initial reversible separation process within a certain separation limit, followed by irreversible damage and separation beyond the limit. A contact detection algorithm and a subsequent contact force model are used for surfaces after fracture. The Coulomb friction damping model is used for surfaces that are in contact. Fourier's heat conduction model is coupled with mechanical deformation and failure models to account for thermal conduction in the material. Details of the cohesive element framework and algorithm and the finite element numerical scheme can be found in Barua and Zhou (2011).

The thermo-mechanical constitutive relations for the constituents are as follows. The stress tenor is decomposed into a hydrostatic part and a deviatoric part, i.e.,

$$\sigma_{ij} = -P\delta_{ij} + \sigma'_{ij}, \tag{1}$$

where σ_{ij} is the Cauchy stress tensor and P is the hydrostatic pressure which is obtained by

$$P = -\frac{1}{3}(\sigma_{11} + \sigma_{22} + \sigma_{33}) = -\frac{1}{3}\sigma_{ii}. \tag{2}$$

In the discussions to follow, the hydrostatic stress is often referred to as "pressure". The Cauchy stress relates to the Kirchhoff stress via

$$\tau_{ij} = J\sigma_{ij}, \tag{3}$$

where $J = \det(\boldsymbol{F})$ is the Jacobian, with $\boldsymbol{F}$ being the deformation gradient. The deviatoric part of the stress tensor carried by the HMX grains follows an elasto-viscoplastic constitutive law and the hydrostatic part follows the Birch–Murnaghan equation of state (B–M EOS).

The deviatoric constitutive behavior of the grains is described by

$$\hat{\boldsymbol{\tau}}' = \boldsymbol{L} : (\boldsymbol{D}' - \boldsymbol{D}'_{\mathrm{p}}), \tag{4}$$

where $\boldsymbol{L}$ is the tensor of elastic moduli and $\hat{\boldsymbol{\tau}}'$ is the deviatoric part of the Jaumann rate of the Kirchhoff stress. For isotropic elastic response,

$$\boldsymbol{L} = 2\mu\tilde{\boldsymbol{I}} + \lambda\boldsymbol{I} \otimes \boldsymbol{I}. \tag{5}$$

Here, $\boldsymbol{I}$ is the second order identity tensor, $\tilde{\boldsymbol{I}}$ is the fourth order identity tensor, λ and μ are Lamé's first and second constants. $\boldsymbol{D}'$ in Eq. (4) is the deviatoric part of the rate of deformation, which can be decomposed into an elastic part and a viscoplastic part as

$$\boldsymbol{D}' = \boldsymbol{D}'_e + \boldsymbol{D}'_p, \tag{6}$$

where $\boldsymbol{D}'_p$ is the viscoplastic part of $\boldsymbol{D}'$ in the form of

$$\boldsymbol{D}'_p = \frac{3\dot{\bar{\varepsilon}}}{2\bar{\sigma}}\boldsymbol{\tau}', \quad with \ \ \bar{\sigma}^2 = \frac{3}{2}\boldsymbol{\tau}' : \boldsymbol{\tau}'. \tag{7}$$

Table 2
Parameters in viscoplastic constitutive model of HMX.

σ_0 (MPa)	ε_0	N	T_0 (K)	β
260	5.88×10^{-4}	0.0	293	0.0
$\dot{\bar{\varepsilon}}_0$ (s^{-1})	m	$\dot{\bar{\varepsilon}}_m$ (s^{-1})	a (1/MPa)	κ
1×10^{-4}	100.0	8.0×10^{12}	22.5	0.0

Here, $\bar{\sigma}$ is the Misses equivalent stress, $\boldsymbol{\tau}'$ is the deviatoric part of the Kirchoff stress, and $\dot{\bar{\varepsilon}}$ is the equivalent plastic strain rate which has the form of

$$\left.\begin{aligned} \dot{\bar{\varepsilon}} &= \frac{\dot{\bar{\varepsilon}}_1 \dot{\bar{\varepsilon}}_2}{\dot{\bar{\varepsilon}}_1 + \dot{\bar{\varepsilon}}_2}, \\ \dot{\bar{\varepsilon}}_1 &= \dot{\bar{\varepsilon}}_0 \left[\frac{\bar{\sigma}}{g(\bar{\varepsilon}, T)}\right]^m, \\ \dot{\bar{\varepsilon}}_2 &= \dot{\bar{\varepsilon}}_m \exp\left[-a\, g(\bar{\varepsilon}, T)\right], \\ g(\bar{\varepsilon}, T) &= \sigma_0 \left(1 + \frac{\bar{\varepsilon}}{\varepsilon_0}\right)^N \left\{1 - \beta\left[\left(\frac{T}{T_0}\right)^\kappa - 1\right]\right\}, \end{aligned}\right\} \tag{8}$$

where $\bar{\varepsilon} = \int_0^t \dot{\bar{\varepsilon}} dt$ is the equivalent plastic strain, $\dot{\bar{\varepsilon}}_0$ and $\dot{\bar{\varepsilon}}_m$ are reference strain rates, m and a are rate sensitivity parameters for a low regime of strain rate and a high regime of strain rate, respectively. The specific range of the regime varies depending on the reference strain rates, $\dot{\bar{\varepsilon}}_0$ and $\dot{\bar{\varepsilon}}_m$. The parameter σ_0 is the quasi-static yield stress, ε_0 is a reference strain, N is the strain hardening exponent, T_0 is a reference temperature, and β and κ are thermal softening parameters. The function $g(\bar{\varepsilon}, T)$ represents the quasi-static stress-strain response at ambient temperature. The above relations consider strain hardening and strain-rate dependence of plasticity. The details of the above constitutive relations and descriptions of the parameters can be found in Zhou et al. (1994). The parameters the plasticity model for HMX used in this study are listed in Table 2. The parameters are calibrated to match the experimental wave profile obtained by Dick et al. (2004). The verification of the calibrated parameters is described in Hardin (2015).

The binders considered are commercially available polymers known as nitrocellulose (NC) used in PBX 9404. The binders follow the Generalized Maxwell Model (GMM) (Mas and Clements, 1996) in the form of

$$\boldsymbol{\sigma}(\tau) = \int_0^\tau 2G\left(t - t'\right) \frac{\partial \boldsymbol{\varepsilon}^D}{\partial t'} dt' + \int_0^\tau K_0\left(t - t'\right) \frac{\partial \boldsymbol{\varepsilon}^H}{\partial t'} dt', \tag{9}$$

where $\boldsymbol{\sigma}$ represents the Cauchy stress, $\boldsymbol{\varepsilon}^D$ and $\boldsymbol{\varepsilon}^H$ refer to the deviatoric and hydrostatic portions of the Eulerian strain tensor, and τ and t refer to physical and reduced times, respectively. The bulk modulus K_0 of the polymer is assumed to be a constant, as in Mas and Clements (1996) and Wu and Huang (2009). The deviatoric part of the constitutive behavior of the polymer binder is described by a Prony series. The shear modulus G is assumed to vary with the relaxation time τ^r in the form of

$$G(t) = G_e + \sum_{i=1}^{n} G_i \exp\left(-\frac{t}{\tau_i^r}\right), \tag{10}$$

where G_e is the long term modulus when the binder is fully relaxed, and τ_i^r and G_i are the relaxation time and the modulus of ith mode, respectively. The modulus of the binder is highly dependent on the temperature and the loading rate. Tucker (2013) measured the storage modulus of the nitrocellulose/plasticizer mixture over a range of stress wave frequencies (10^{-8}–10^8 Hz) and temperatures (223–323 K). The frequency-modulus relations for different temperatures are shifted and superposed by using the Williams–Landell–Ferry (WLF) shift function with the form of

$$\log(a_T) = \frac{-C_1 (T - T_0)}{C_2 + (T - T_0)}. \tag{11}$$

A master curve for the storage modulus $G'(\omega)$ is obtained for all temperatures, as shown in Fig. 10-10 in Tucker (2013). Mas et al. (2002) showed that the storage modulus $G'(\omega)$ can be represented in terms of the Prony series parameters by using the equation of

$$G'(\omega) = G_e + \sum_{i=1}^{n} G_i \frac{\omega^2 \left(\tau_i^r\right)^2}{1 + \omega^2 \left(\tau_i^r\right)^2}, \tag{12}$$

where $\tau_i^r = 1.5 a_T / \omega$ as in Mas et al. (2002). We use the 17-element series for NC. Specifically, we choose 17 points along the modulus line from 10^{-8} Hz to 10^8 Hz in Fig. 10-10 of Tucker (2013) as shown in Fig. 3, and convert the 17 moduli values to the Prony series parameters as tabulated in Table 3 for the binder of PBX 9404.

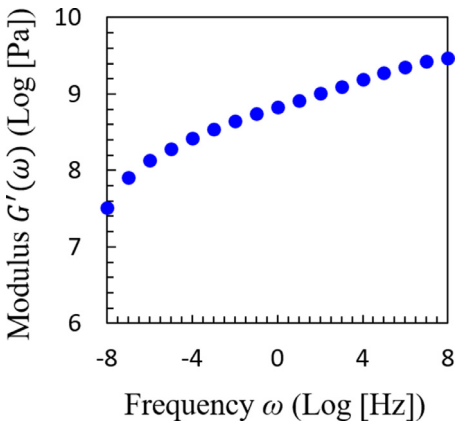

Fig. 3. Modulus of the binder of PBX 9404 (Tucker, 2013).

Table 3
Parameters of the Prony series for NC binder in PBX 9404.

Frequency (Hz)	G_i (MPa)	Frequency (Hz)	G_i (MPa)
10^{-8}	45.52	10^{1}	169.9
10^{-7}	50.12	10^{2}	204.5
10^{-6}	55.19	10^{3}	249.3
10^{-5}	59.53	10^{4}	299.4
10^{-4}	75.63	10^{5}	361.6
10^{-3}	84.48	10^{6}	381.8
10^{-2}	96.22	10^{7}	387.0
10^{-1}	113.0	10^{8}	320.6
1	126.4		$G_e = 0$

WLF parameters: $C_1 = 165$, $C_2 = 960$, $T_0 = 273$ K from Tucker (2013)

The volumetric part of the stress tensor is described by the Birch–Murnaghan equation of state (B–M EOS). The specific form of the equation is

$$\tau_h = \frac{3}{2}K_0 J\left(J^{-\frac{7}{3}} - J^{-\frac{5}{3}}\right)\left[1 + \frac{3}{4}\left(K'_0 - 4\right)\left(J^{-\frac{2}{3}} - 1\right)\right], \tag{13}$$

where $\tau_h = \tau_{ii} = \tau_{11} + \tau_{22} + \tau_{33}$ is the hydrostatic part of the Kirchoff stress, which is the product of the Jacobian and the negative of the hydrostatic pressure. K_0 is the bulk modulus, and $K'_0 = (\partial K_0/\partial P)_{P=0}$. For the implementation of the B–M EOS, a time incremental form of the above is used. Since the time rate of change of the Jacobian is

$$\frac{\partial J}{\partial t} = J\,\mathrm{tr}(\boldsymbol{D}), \tag{14}$$

the rate of change of the hydrostatic Kirchhoff stress is only a function of the Jacobian and rate of deformation, i.e.,

$$\frac{\partial \tau_h}{\partial t} = f\left(\frac{dV}{dV_0}, \mathrm{tr}(\boldsymbol{D})\right). \tag{15}$$

This relation, details of which are obtained by differentiating Eq. (13), is needed in evaluating the responses of the constituents.

Previous studies (Gump and Peiris, 2005; Yoo and Cynn, 1999; Landerville et al., 2010) show discrepancies in the parameters of B–M EOS for HMX. Landerville et al. (2010) reported that the parameters vary to a large degree among experiments due to inherent noise of experiments and inconsistencies in fitting ranges and schemes. The parameter values used in this study are $K_0 = 16.71$ GPa and $K'_0 = 7.79$ as reported in Landerville et al. (2010) which lie in between the values of Gump and Peiris (2005) and Yoo and Cynn (1999). Fig. 4(a) shows the pressure–volume relations from the B–M EOS model (Landerville et al., 2010) and the experimental data of HMX (Marsh, 1980).

The pressure–volume relation for the binder of PBX 9404 is estimated from the Hugoniot data of cellulose acetate in Marsh (1980) with the replacement of the density by 1.65 g/cm^3. The same estimation based on cellulose acetate properties was made by Swift et al. (2002) and Moore et al. (2007). The parameters of B–M EOS for the NC binder of PBX 9404 is obtained by a curve fitting of the pressure–volume Hugoniot data as shown in Fig. 4(b). The parameters of the B–M EOS for HMX and the binders of PBX 9404 (NC) are listed in Table 4.

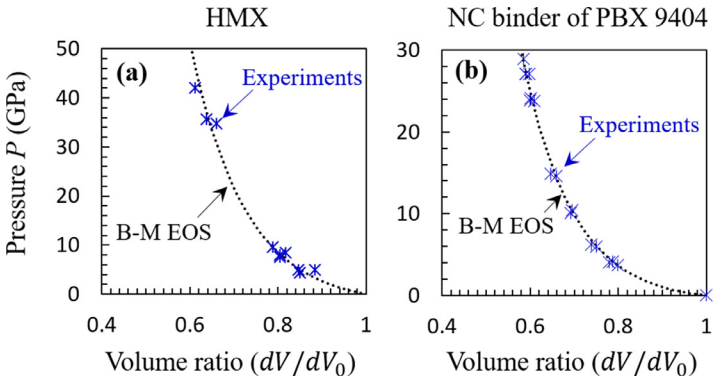

Fig. 4. Hugoniot P–V relations of (a) HMX, and (b) NC binder estimated from cellulose acetate. The vertical axes of all figures have the same unit as shown in the left most plot. The experimental data for HMX and NC are from Marsh (1980).

Table 4
Parameters of B–M equation of state for HMX and NC binder.

Parameters	HMX	NC
K_0 (GPa)	16.71	5.797
K_0'	7.79	10.61

Table 5
Material properties of HMX and NC binder.

Properties	HMX	NC
Density ρ (kg· m^{-3})	1910 (Saw, 2002)	1650 (Swift et al., 2002)
Specific Heat c_p (kJ· kg^{-1}· K^{-1})	1.254 (Shoemaker et al., 1985)	2.350 (Rajic and Suceska, 2000)
Thermal conductivity k (W· m^{-1}· K^{-1})	0.52 (Gonthier, 2003; Wemhoff et al., 2007)	0.3138 (Miller, 1997)
Ratio of heat dissipation from plastic deformation	0.9 (Hodowany et al., 2000)	N/A

Temperature in the material under dynamic loading rises locally due to plastic dissipation, viscoelastic dissipation, frictional dissipation along interfaces, and heat conduction. The specific form of the heat equation is

$$\rho c_p \frac{\partial T}{\partial t} = k\nabla^2 T + \eta \dot{W}^p + \dot{W}^{ve} + \dot{W}^{fric} \tag{16}$$

where ρ is density, c_p is specific heat, T is temperature, t is time, k is thermal conductivity, η is the fraction of plastic work that is converted into heat, $\dot{W}^p$ is the rate of plastic work per unit volume, $\dot{W}^{ve}$ is the rate of viscoelastic dissipation per unit volume, and $\dot{W}^{fric}$ is the rate of frictional dissipation per unit volume. For a volume element ΔV that contains a total area of ΔS of internal frictional surface pairs,

$$\dot{W}^{fric} = \frac{1}{\Delta V}\int_{\Delta S} \mu \sigma_n v_{rel} dS, \tag{17}$$

where μ is the coefficient of friction, σ_n is the normal force on the contact surface pair, and v_{rel} is the relative sliding velocity at the contact surface. Table 5 shows the parameters of the ratio of plastic work converted into heat (η), density (ρ), specific heat (c_p), and thermal conductivity (k) for HMX and the binder of PBX 9404.

Arbitrary fracture patterns inside the individual constituents and interfacial debonding between particles and the binder are explicitly captured by the use of cohesive elements embedded throughout the finite element model. The cohesive elements follow a bilinear traction separation law described by Zhai et al. (2004). The cohesive relation embodies an initial reversible separation processes with a certain separation limit, followed by irreversible damage and separation beyond the limit. If the separation reaches a critical distance, the cohesive surface pair is considered as failed, and no stress is applied for further separation. A verification of the cohesive element framework is provided in Barua and Zhou (2011).

The formation of a crack (inside a constituent or along a grain-binder boundary) results in the creation of two surfaces. At each computational time step, the entire domain is scanned and such surfaces are identified. The corresponding nodal coordinates of all possible pairs of surfaces are compared to detect surface contact and overlap. Penalty forces are applied to strongly discourage interpenetration and maintain proper contact of the surfaces. Detailed descriptions of the multi-step contact algorithm and the penalty forces are given in Hardin (2015). Frictional heating, due to sliding along surfaces in contact, is assessed using the Coulomb friction law. The stick-slip state is determined by the normal force between the contact surface pair. Green et al. (1971) obtained the frictional coefficient of approximately 0.3–0.7 for PBX9404, and Chidester et al. (1993) used the coefficient of 0.5 as the average value of Green et al. (1971). In this analysis, we also used the frictional coefficient of 0.5 for fractured surfaces in PBX 9404.

2.4. Hotspot-based initiation criterion

The size and temperature of hotspots need to be quantified prior to the application of any threshold criteria for ignition. For each load intensity and loading duration, temperature fields from early on until after the shock pulse diminishes in the sample, of the entire sample are scanned. Areas of each temperature field with temperatures above a given threshold (T_{thres}) are analyzed for hotspots. Specifically, the temperature field is converted to a binary on/off (or black/white) map where only the areas with $T > T_{thres}$ are of interest and are marked "on". Each "on" area representing a hotspot having arbitrary size and shape. The size of the hotspot is calculated as the diameter of a circle with the same area as the hotspot. This equivalent diameter scheme provides an effective method to capture the hotspot characteristics. Using this method, a list of hotspots and equivalent diameters is obtained for each T_{thres}. Successively varying T_{thres} values allows the characteristics of the whole temperature field to be fully analyzed. An example of the hotspot size-temperature characteristics for a range of temperature can be seen in Fig. 6 of Barua et al., 2013b.

After all hotspots in a sample are quantified in terms of size and temperature, a criterion for initiation is used to determine the onset of irreversible chemical decomposition of HMX in the samples. This criterion provides a relationship between the size and the temperature states of critical hotspots. Specifically,

$$d(T) \geq d_c(T), \tag{18}$$

where d is the diameter of a hotspot resulting from a loading event whose interior temperatures are at or above temperature T. d_c is the minimal diameter of a hotspot required for thermal runaway at temperature T. The quantitative information regarding the right-hand side of Eq. (18) is taken from the work of Tarver et al. (1996) who performed chemical kinetics calculations to analyze the criticality issue for HMX and TATB explosives. The calculations consider multistep reaction mechanisms, including the pressure and temperature dependence of reactants and products. More details about the initiation criterion can be found in Barua et al. (2013a).

The left-hand side of Eq. (18) is obtained by analyzing the temperature fields in the microstructures from CFEM calculations. To account for the variations of temperature within a hotspot (note that temperatures at different spatial locations within a hotspot are different and the temperature threshold is the lowest temperature at the periphery), the hotspot threshold of Tarver et al. is treated as a band of ±10% about the mean value, as in Barua et al. (2013a). A hotspot is considered to be critical when it crosses the lower threshold limit (90% of the average value). The initiation of the material is regarded as being reached if the critical hotspot density is equal to or greater than 0.22 mm^{-2} which corresponds to two critical hotspots in a 3 mm square domain. The specific choice of the current critical hotspot density (0.22 mm^{-2}) is based on the observation of Barua et al. (2013a) who found a negligible difference on the criticality results by changing the critical hotspot density between 0.11 mm^{-2} (single hotspot in a 3 mm square domain) to 0.44 mm^{-2} (4 hotspots in a 3 mm square domain). This consistency is primarily because many hotspots develop simultaneously and reach the threshold within very short time intervals from each other.

Once the hotspots reach criticality, energy released by chemical reaction in the hotspots dominates and eventually leads to detonation, provided that there is no quenching of chemistry due to unloading caused by rarefaction from nearby free boundaries. The focus here is on conditions that allow hotspots to reach criticality and, therefore, the sample to reach ignition which ultimately leads to detonation. This study does not consider the process of how critical hotspots result in detonation. Such a study is unnecessary for the purpose of this paper, as there is a one-to-one correspondence between initiation and eventual detonation, as discussed in the Introduction. It has been contemplated that interactions among subcritical hotspots in close proximity of each other might lead to one critical hotspot or criticality. There has been no research on this subject. If a critical hotspot is to emerge from the interactions of multiple hotspots, it would be detected by the approach used here and accounted for by the ignition criterion. The possibility of multiple hotspots leading to ignition without first producing a critical hotspot, although not having been positively demonstrated, can be the subject of a future study.

3. Results and discussion

The predictive calculations are performed in the following steps. First, a set of statistically similar samples having computationally generated microstructures as described in Section 2.1 are subject to one of the loading conditions discussed in Section 2.2. Second, at a preset time interval, the initiation criterion described in Section 2.4 is used to identify critical hotspots that have reached the size-temperature ignition threshold. A sample reaches criticality if it has a sufficient number of critical hotspots as stated in Section 2.4. Third, the loading conditions required for a 50% ignition probability are determined. Based on the 50% ignition probability line, two types of ignition threshold are established – one type from the Walker–Wasley equation (Walker and Wasley, 1969) and the other type from the James equation (James, 1996). Finally, the two types of threshold are modified to establish the initiation probability over the entire range of loading space.

3.1. Stress attenuation and hotspot distribution

As a shock wave propagates through a material, stress decreases and temperature increases due to energy dissipation from material inelasticity and friction along crack interfaces. Fig. 5(a) shows the temperature field in the initial 3×3 mm^2 area near the impact face of a PBX 9404 sample subjected to loading with $U_p = 800$ m/s and $\tau = 125$ ns at $t = 1.6$ μs. The

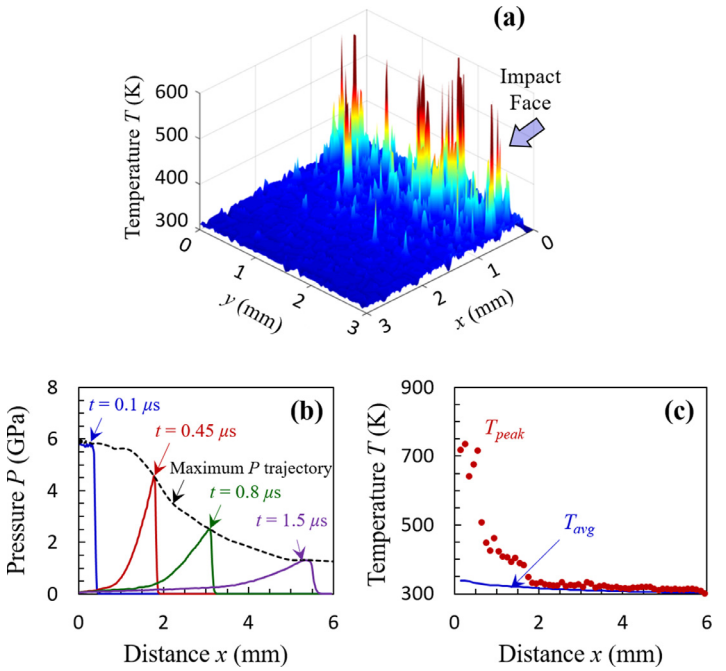

Fig. 5. (a) Temperature field in the 3×3 mm^2 section near the impact surface of a 3×15 mm^2 domain at $t = 1.6$ μs, (b) trajectory of peak pressure, and (c) corresponding temperature profile at $t = 1.6$ μs for a PBX 9404 sample under loading with $U_p = 800$ m/s and $\tau = 125$ ns.

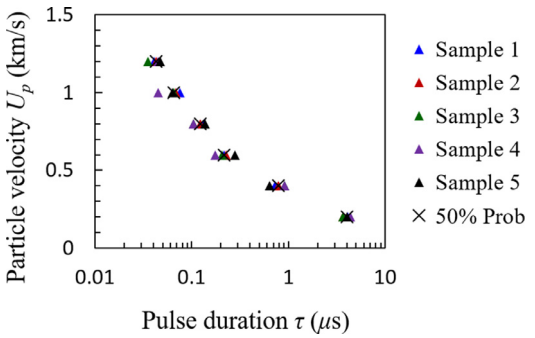

Fig. 6. Minimum pulse durations required for initiation predicted from five PBX 9404 samples and the durations for 50% ignition probability. The samples used have statistically similar microstructures.

hotspots are concentrated near the impact surface and rapidly disappear as the distance from the impact face increases. Fig. 5(b) shows the pressure profiles at different times with the peak pressure trajectory outlined. Fig. 5(c) shows the peak and average temperature profiles at $t = 1.6$ μs. Clearly, the peak temperature follows the pattern of the peak pressure as a function of distance from the impact face.

Five statistically equivalent samples are computationally analyzed at each load intensity (or imposed particle velocity at the impact face). Due to the inherent material heterogeneities, different samples require slightly different pulse durations to reach the ignition threshold. Although different samples have statistically equivalent microstructural attributes, random grain shapes and grain distributions cause the samples to have local fields that fluctuate randomly, thereby giving rise to slightly different behaviors. As an example, Fig. 6 shows the minimum pulse duration required for initiation for each sample of PBX 9404. The symbol '×' demarcates the threshold for 50% probability of initiation as determined by all samples over the entire load regime analyzed. The scatter of data relative to the 50% probability threshold indicates the statistical variations of ignition behavior arising out of random microstructure fluctuations. More detailed analysis is performed using the normal and log-normal distribution functions later.

As seen in Fig. 5(b), the pressure pulse attenuates as it propagates through the material, generating hotspots along the way. As load intensity increases, shorter durations of loading is required for ignition. Short pulses have faster delays and narrower spatial bands of hotspot distributed near the impact surface. The temperature rise is affected by the stress attenuation under various combinations of shock intensity and pulse duration required for the 50% initiation probability.

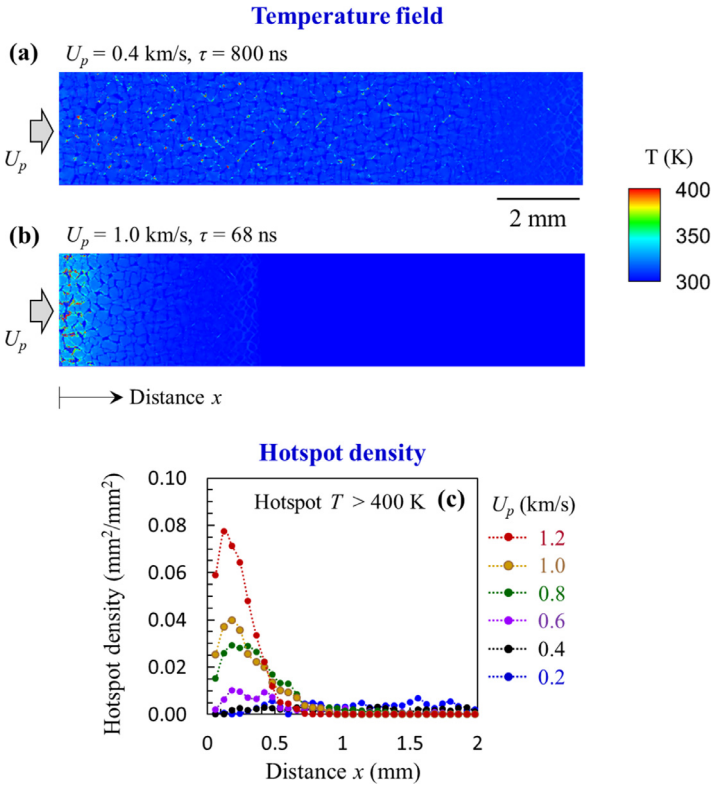

Fig. 7. (a–b) Temperature field for PBX 9404 under shock loading with (a) $U_p = 0.4$ km/s and $\tau = 800$ ns and (b) $U_p = 1$ km/s and $\tau = 68$ ns. The pulse durations chosen correspond to 50% ignition probability. (c) Profiles of hotspot density with hotspots having $T > 400$ K for PBX 9404 samples under shock loading with $U_p = 0.2$–1.2 km/s and the corresponding pulse durations yielding a 50% ignition probability.

Fig. 7(a–b) shows two temperature fields for PBX 9404, one for a low load intensity but long pulse duration ($U_p = 0.4$ km/s and $\tau = 800$ ns) and the other a high load intensity but short duration ($U_p = 1.0$ km/s and $\tau = 68$ ns). The case with low load intensity has hotspots dispersed over a half of the sample length of 15 mm. On the other hand, the case with high load intensity has hotspots very close to the impact surface. Fig. 7(c) shows the hotspot density profiles. In Fig. 7(c), the sample domain is divided into fine strips (180 μm in width) perpendicular to the loading direction and each dot ('•') in the figure represents the average value of a given strip. The curves are the connected lines of the average values of all strips. This same approach is used to graph the variation of other quantities along the loading direction later in Figs. 8, 15, 16, and 17 as well. A cutoff temperature of $T_{cut} = 400$ K is used to define hotspots. Since a higher load intensity results in more hotspots, a proper cutoff temperature should be set to obtain meaningful trends. Barua et al. (2013c) used a cutoff temperature of $T_{cut} = 320$ K under low-intensity impact ($U_p = 50$ m/s), and analyzed the effect of volume fraction, confinement, and overall strain. Gilbert et al. (2013) used a cutoff temperature of $T_{cut} = 500$ K under high-intensity monotonic loading ($U_p = 100$–500 m/s). Here, the imposed loading has higher intensities and short pulse durations, as a result a cutoff temperature of $T_{cut} = 400$ K is used. The same cutoff temperature was used previously (Kim et al., 2014, 2015). The area of hotspots is analyzed over the load range of $U_p = 0.2$–1.2 km/s for the pulse durations corresponding to the 50% ignition probability in Fig. 6. Fig. 8 shows the profiles of overall energy dissipation (Fig. 8(a)) and the profiles of dissipations due to friction (Fig. 8(b)) or plastic deformation (Fig. 8(c)). The energy dissipated under high-intensity loading is localized in the narrow region near the impact surface. As the load intensity decreases and the pulse duration increases, the energy dissipated is more widely distributed, impeding hotspot development and requiring more overall input energy for hotspots to reach criticality or the sample to reach ignition. The relationship between critical input energy and load intensity is analyzed later. Overall, the trend of hotspot density (Fig. 7(c)) is similar to the trend of energy dissipations (Fig. 8). However, as the load intensity decreases, hotspot density decreases significantly, more than the decrease in the energy dissipated. For example, for $U_p = 1.2$ km/s and 0.4 km/s, the maximum energy dissipated decreases to 1/4 of the higher value (from 0.13 kJ/cm^3 to 0.034 kJ/cm^3), whereas the maximum hotspot density decreases to 1/25 of the higher value (from 0.078 mm^2/mm^2 to 0.003 mm^2/mm^2). Fig. 9(a) shows the maximum hotspot density as a function of load intensity in the form of power flux (Π) which is the rate at which energy is imparted to the sample per unit area of the impact face. The power flux can be obtained from the hydrostatic pressure and particle velocity via $\Pi = PU_P$. The results in Fig. 9(a) show that the highest hotspot density increases linearly with Π. The location from the impact face at which the highest hotspot density occurs decreases with Π, as shown in Fig. 9(b).

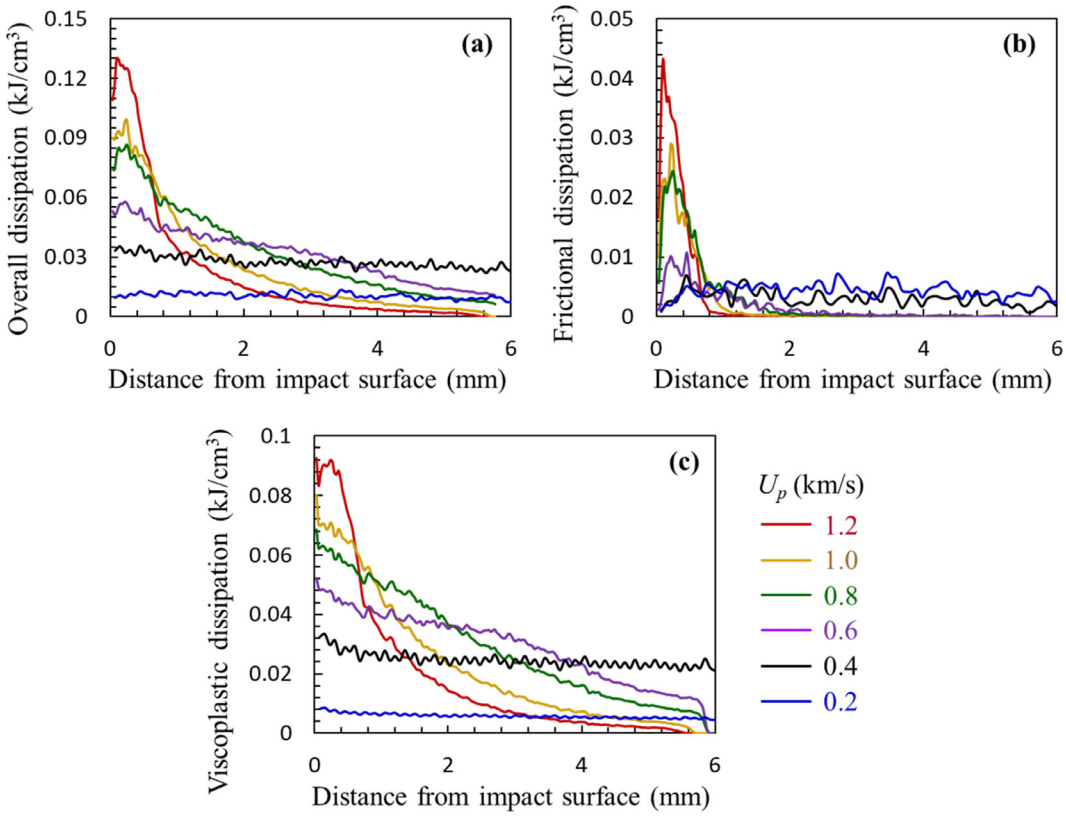

Fig. 8. For PBX 9404 samples under shock loading with $U_p = 0.2$–1.2 km/s and the corresponding pulse durations yielding a 50% ignition probability: profiles of (a) overall energy dissipation, (b) dissipation due to friction, and (c) dissipation due to plastic deformation.

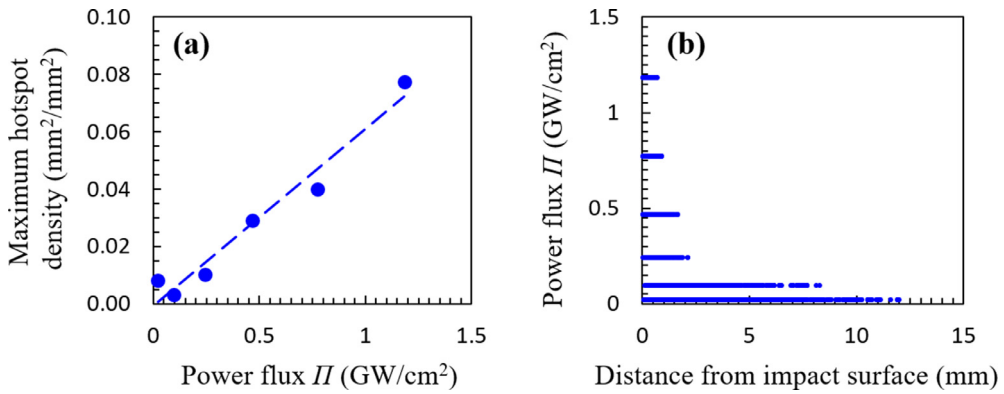

Fig. 9. For PBX 9404 samples under shock loading with $U_p = 0.2$–1.2 km/s and the corresponding pulse durations yielding a 50% ignition probability, (a) highest hotspot density in the samples and (b) distance from the impact surface at which the highest hotspot density is observed for the different load intensities as measured by the power flux. Hotspots with $T > 400$ K are considered.

3.2. Walker–Wasley type and James type ignition thresholds

Predicted initiation thresholds with 50% probability are further analyzed using two types of well-known initiation threshold functions proposed by Walker and Wasley (1969) and James (1996). The Walker–Wasley threshold is expressed in terms of load pressure (P) and load duration (τ). The specific form is

$$P^2\tau = C\,, \tag{19}$$

where C is a material-dependent fitting parameter. The original James threshold is expressed in terms of the input energy ($E = PU_p\tau$) and the load intensity in the form of the specific kinetic energy ($\Sigma = 0.5U_P{}^2$). Recently, Welle et al. (2014a) modified the James threshold by replacing the specific kinetic energy with the power flux ($\Pi = PU_P$), a measure for the rate at

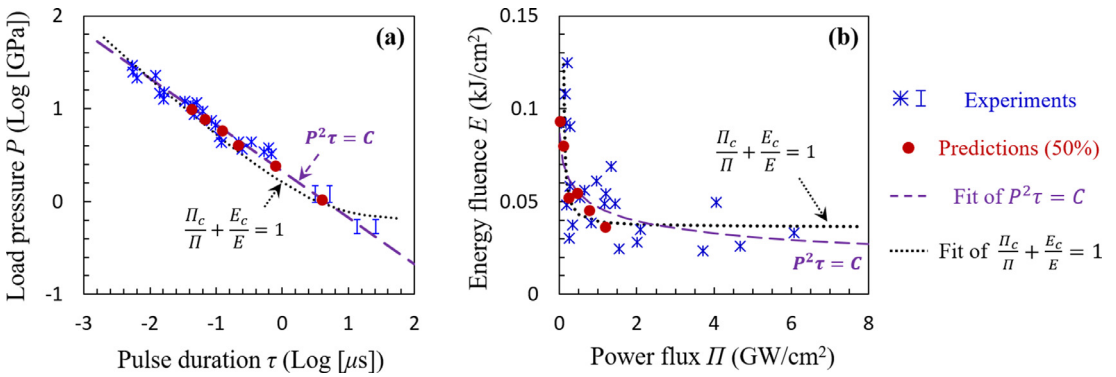

Fig. 10. Thresholds for 50% probability of initiation obtained from computational predictions and experiments reported in the literature ('✳' from Weingart et al., 1980 and '⌶' from Hayes, 1976), (a) in the P–τ space and (b) in the E–Π space. The purple dash lines (- - -) represent the Walker–Wasley relation ($P^2\tau = C$) and the black dotted lines (···) represent the James relation ($\Pi_c/\Pi + E_c/E = 1$). The results primarily concern PBX 9404.

Table 6
Parameters in Walker–Wasley and James initiation thresholds.

	C (10^{12} Pa$^2\cdot$ s)	Π_c (GW/cm^2)	E_c (kJ/cm^2)
Experiments (Hayes, 1976; Weingart et al., 1980) (PBX 9404)	4.58	0.0997	0.0345
Predictions (PBX 9404)	4.09	0.0115	0.0474

which work imparted to the material per unit area of the impact face. The resulting form is

$$\frac{\Pi_c}{\Pi} + \frac{E_c}{E} = 1\,, \tag{20}$$

where E_c and Π_c are fitting parameters which represent asymptotic thresholds for the critical energy and the critical power flux, respectively. The input energy (E) is the time integration of the power flux (Π) over the pulse duration.

Fig. 10(a) shows a comparison in the P–τ space of the experimentally measured and computationally predicted thresholds for PBX 9404 with an initiation probability of 50%. The experimental data is from Hayes (1976) and Weingart et al. (1980). Fig. 10(b) shows a representation of the same data set shown in Fig. 10(a) in the E–Π space. The purple dash line in Fig. 10(a–b) represents fits of the experimental data for PBX 9404 to the Walker–Wasley relation in Eq. (19). The black dotted line in Fig. 10(a–b) represents fits of the experimental data for PBX 9404 to the modified James relation in Eq. (20). For this figure, the Hugoniot of PBX9404 obtained by Roth (1970) is used to convert the pressure of the experimental data to particle velocity (U_p). Overall, the computationally predicted initiation threshold of PBX 9404 is in good agreement with that observed in experiments.

The vales for parameters C, E_c, and Π_c obtained from the experimental data and the predictions are listed in Table 6. Both the James relation and the Walker–Wasley relation capture the overall trend of the initiation data for PBX 9404 very well. However, this is not always the case for other types of explosives. For example, the initiation thresholds of TATB and PBX consisting of TATB and a binder are better represented by the James relation than the Walker–Wasley relation as shown in James (1996) and Honodel et al. (1981).

3.3. Ignition probability map

As shown in Fig. 10(b), there exists a significant scatter of data points in both experiments and computations. The data points are for different samples of the same materials. In general for experiments, the data points are for different specimens out of the same material batch. For the computations here, the data points are for multiple samples with statistically similar microstructures, mimicking the multiple specimens in experiments. The scatter may be attributed to, as pointed out by Gresshoff and Hrousis (2010), uncertainties from experimental conditions and random heterogeneities in the specimens. While both types of randomness exist in the experiments, the simulations here consider the effects of inherent heterogeneities in the samples. The threshold lines represented by Eq. (19) and Eq. (20) in Fig. 10(a–b) indicate the loading conditions for a 50% probability of ignition. Additionally, Gresshoff and Hrousis (2010) combined the James criterion with an assumption about the initiation probability distribution (scatters due to the two types of uncertainty) by introducing the James number, J. This number, defined in Eq. (21), serves as a metric to define the safety and performance margins in a probabilistic fashion. Specifically,

$$\frac{\Pi_c}{\Pi} + \frac{E_c}{E} = \frac{1}{J}\,, \tag{21}$$

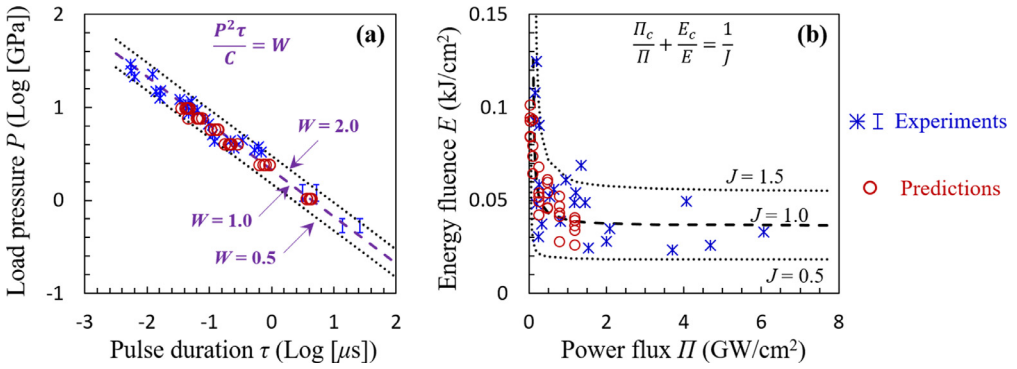

Fig. 11. (a) Modified Walker–Wasley relation with $W = 0.5$, 1.0, and 2.0 and (b) modified James relation with $J = 0.5$, 1.0, and 1.5 for PBX 9404. Experimental data marked as '✳' are from Weingart et al. (1980) and '⌶' are from Hayes (1976).

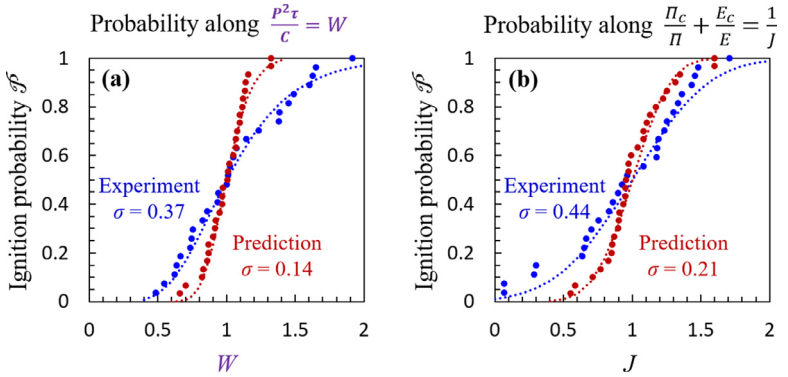

Fig. 12. The ignition probability function of (a) W with a log-normal distribution fit and (b) J with a normal distribution fit for PBX 9404. Both experimental results and computational predictions are shown.

where $J = 1$ yields the James relation in Eq. (20), $J > 1$ corresponds to loading conditions resulting in ignition probabilities greater than 50%, and $J < 1$ corresponds to conditions resulting in ignition probabilities less than 50%. Using the same approach, we introduce the Walker–Wasley number, W, to quantify the probability of ignition likelihood in the P–τ space via the modified relation

$$\frac{P^2\tau}{C} = W\,, \tag{22}$$

where $W = 1$ yields the Walker–Wasley relation as in Eq. (19), $W > 1$ corresponds to loading conditions resulting in ignition probabilities greater than 50%, and $W < 1$ corresponds to conditions resulting in ignition probabilities less than 50%. As an example of the application of Eq. (21) and Eq. (22), we show in Fig. 11(a–b) the lines corresponding to three levels of ignition probability. These lines are based on the modified Walker–Wasley relation with $W = 0.5$, 1.0, and 2.0 and the modified James relation with $J = 0.5$, 1.0, and 1.5, respectively. Each level of the W and J numbers accounts for all combinations of the loading conditions (i.e., pressure and pulse duration for W and energy fluence and power flux for J) that result in the specified probability of ignition. For example, $W = 0.5$ and $J = 0.5$ for the experimental data correspond to the ignition probability of $\mathcal{P} = 0.03$ and $\mathcal{P} = 0.13$, respectively.

Fig. 12(a–b) shows a comparison of the experimentally determined and computationally predicted ignition probabilities as a function of W or J for PBX 9404. Under the assumption that the scatter of the data points (and, therefore, probability distribution) about the threshold line for $W = 1$ is symmetric in Fig. 11(a) on a log-log scale, a log-normal distribution function $\mathcal{P}(W)$ exists for the initiation probability around a median value of $W = 1$. The specific form of the function is

$$\mathcal{P}(W) = \frac{1}{\sigma\sqrt{2\pi}} \int_{-\infty}^{W} \frac{1}{x} \exp\left[-\frac{(\ln x)^2}{2\sigma^2}\right] dx = \frac{1}{2}\left[1 + \mathrm{erf}\left(\frac{\ln W}{\sqrt{2}\sigma}\right)\right], \tag{23}$$

where σ is the standard deviation. By combining Eqs. (22) and (23), we can obtain a direct relation between the ignition probability P and loading condition parameters P and τ in the form of

$$\mathcal{P}(P,\tau) = \frac{1}{2} + \frac{1}{2}\mathrm{erf}\left[\frac{1}{\sqrt{2}\sigma}\left(\ln(P^2\tau) - \ln C\right)\right]. \tag{24}$$

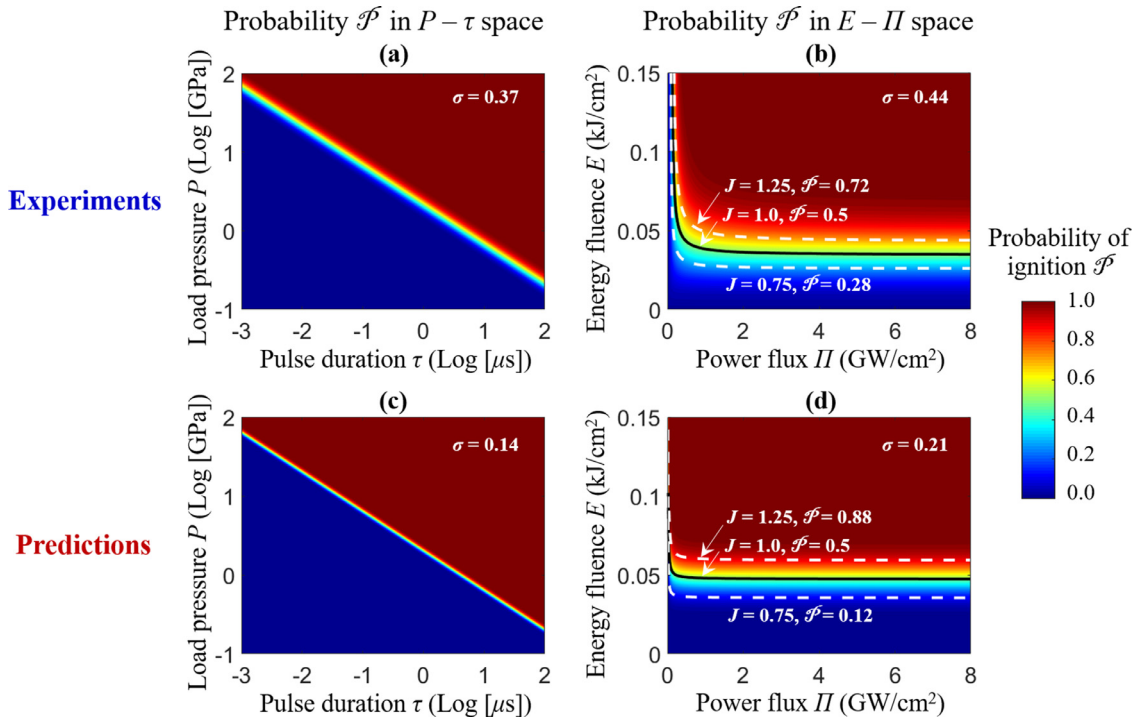

Fig. 13. Ignition probability distribution maps, (a–b) as obtained from experiments in the (a) pressure-pulse duration (P–τ) space and (b) energy fluence-power flux (E–Π) space, and (c–d) as predicted from simulations in the (c) pressure-pulse duration (P–τ) space and (d) energy fluence-power flux (E–Π) space.

Table 7
Standard deviations presented in Fig. 12(a–b).

	Log-normal distribution along $P^2\tau/C = W$	Normal distribution along $\Pi_c/\Pi + E_c/E = 1/J$
Experiments (Hayes, 1976; Weingart et al., 1980) (PBX 9404)	0.37	0.44
Predictions (PBX 9404)	0.14	0.21

Similarly, the initiation probability in the E–Π space as shown in Fig. 11(b) is analyzed using a normal distribution function $\mathcal{P}(J)$. Again, under the condition that the scatter of the data about the threshold line for $J=1$ is symmetric on a linear scale, the initiation probability can be expressed in terms of J and E and Π, respectively, as

$$\mathcal{P}(J) = \frac{1}{\sigma\sqrt{2\pi}}\int_{-\infty}^{J}\exp\left[-\frac{(x-1)^2}{2\sigma^2}\right]dx = \frac{1}{2}\left[1+\mathrm{erf}\left(\frac{J-1}{\sqrt{2}\sigma}\right)\right], \text{ and} \tag{25}$$

$$\mathcal{P}(E,\Pi) = \frac{1}{2}+\frac{1}{2}\mathrm{erf}\left[\frac{1}{\sqrt{2}\sigma}\left(\frac{E\Pi}{\Pi E_c + E\Pi_c}-1\right)\right]. \tag{26}$$

In Eqs. (23)–(26), the standard deviation σ, Walker–Wasley parameter C, cutoff energy fluence E_c and cutoff power flux Π_c are material constants whose values are determined by either experiments or computations reported here. The results are given in Table 6. Once these parameters are determined for a material, the probability of ignition $P(J)$ under any loading condition as measured by P and τ or E and Π can be calculated directly from Eq. (24) or Eq. (26). The material-dependent ignition probability maps obtained from Eq. (24) and (26) are shown in Fig. 13.

The standard deviation values obtained from the samples in Fig. 12(a–b) and those from experiments are listed in Table 7. Overall, the computationally predicted standard deviations are smaller than experimentally determined values. The difference may be attributed to the following factors. First, loading parameters such as pulse duration and impact velocity are precisely controlled in the simulations than in the experiments – experimental uncertainties among multiple tests are not considered in the simulations. Second, the experimental data shown in this paper are the collection of work by multiple groups of researchers (Weingart et al., 1980; Gittings, 1965; Trott and Jung, 1970) as presented in Weingart et al. (1980) and of Christiansen and Taylor (1973) as presented in Hayes (1976). The multiple sources of specimens and test equipment contribute to variations in data. Third, while the specimens in the experiments were not statistically analyzed, the samples in the simulations are generated in a statistically equivalent manner with prescribed level of consistencies. It is certainly to

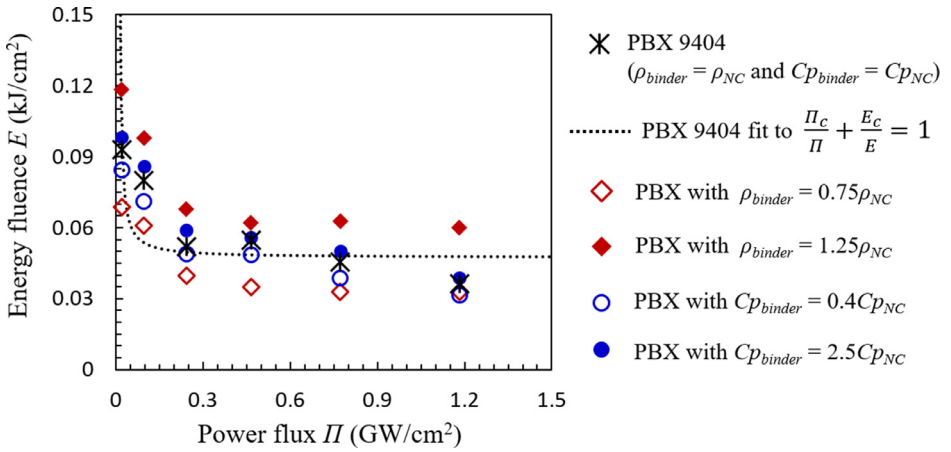

Fig. 14. Comparison of thresholds for 50% probability of initiation in the E–Π space for PBX 9404 and variations of PBX 9404 with different binder properties.

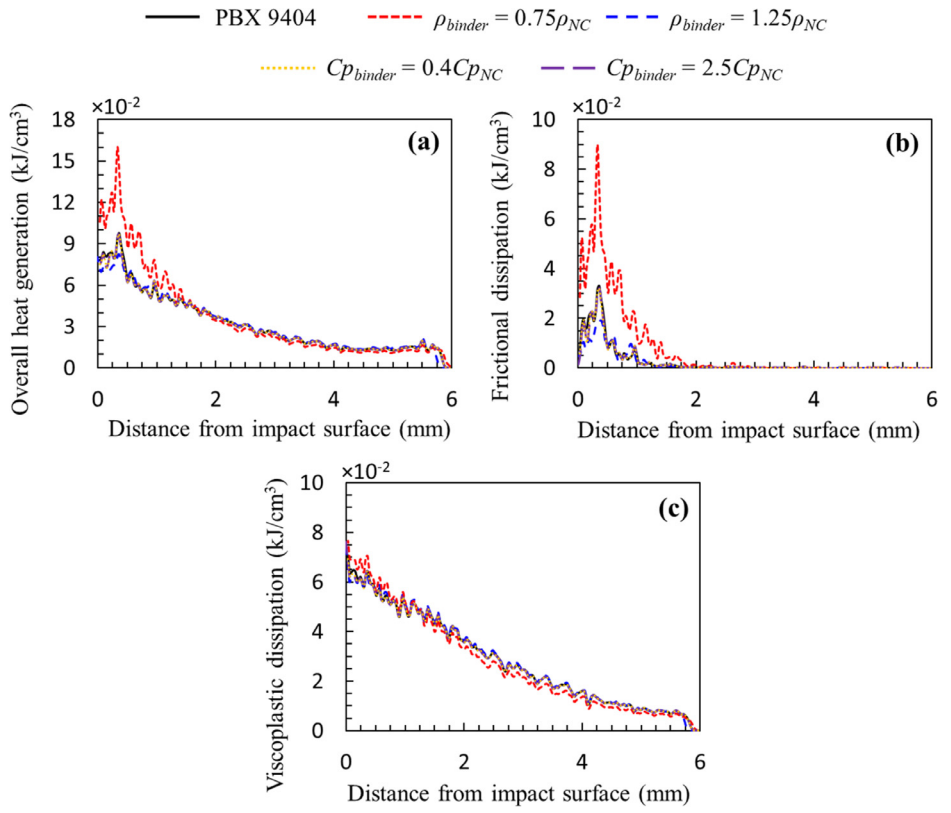

Fig. 15. Profiles of energy dissipations that contribute to temperature changes in PBX 9404 and variations of PBX 9404 with different binder properties: (a) overall heat generation, (b) frictional dissipation, and (c) viscoplastic dissipation. $U_p = 800$ m/s, $\tau = 120$ ns, and $\Delta t = 1.6$ μs.

consider these factors in the future. In particular, uncertainty and variations in loading for different samples can be considered in simulations. Statistical variations and consistency among specimens can be systematically analyzed in experiments for better quantification and comparison with simulations.

3.4. Effect of binder properties on shock sensitivity

PBXs with the same type and amount of energetic granules (grains) but different binders can exhibit significantly different levels of shock sensitivity (Vandersall et al., 2010; Chidester et al., 1998). To delineate the primary factors contributing to the difference, the mechanical and thermal properties of binder in the materials analyzed here are systematically varied

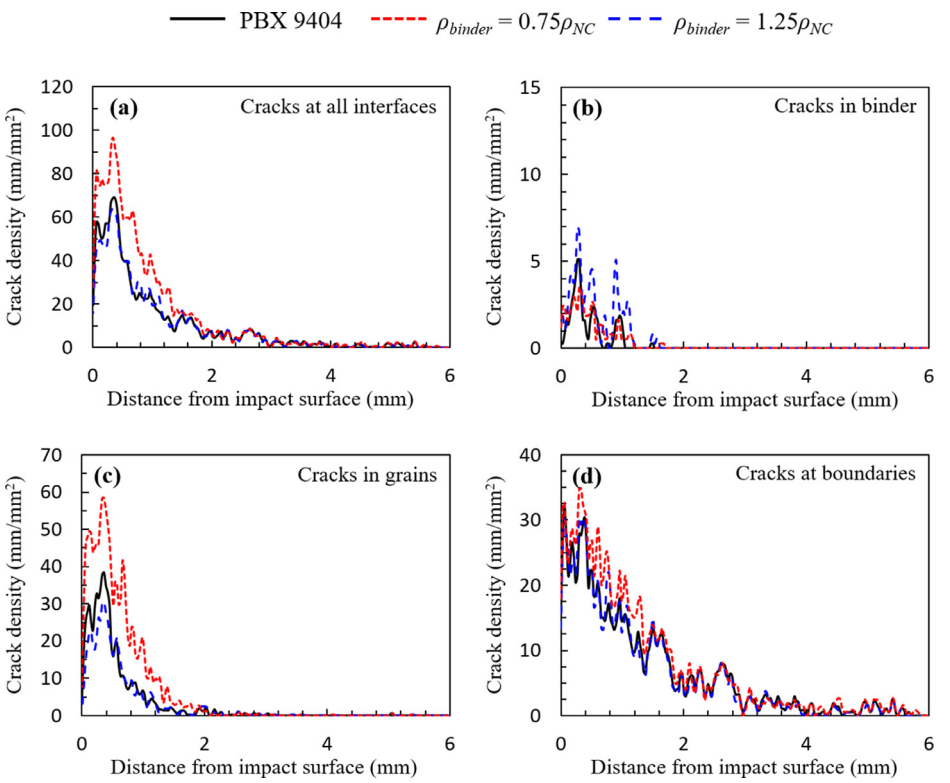

Fig. 16. Profiles of crack density for PBX 9404 and variations of PBX 9404 with different binder mass density values: (a) at all interfaces, (b) in a binder, (c) in grains, and (d) at grain-binder boundaries. $U_p = 800$ m/s, $\tau = 120$ ns, and $\Delta t = 1.6$ μs.

from the properties of the NC listed in Tables 3, 4, and 6. To this effect, a parametric study is carried out with each parameter varied independently of the others under otherwise the same conditions. The resulting James threshold for each calculation set with only one parameter varied is plotted in Fig. 14. Among all parameters considered, binder density and specific heat have the most profound influence on the ignition threshold, with higher binder density and specific heat giving rise to higher ignition threshold.

This trend is not surprising and can be explained by looking temperature change via Eq. (16). The local temperature change over the time period Δt is

$$\Delta T \approx \frac{\int_t^{t+\Delta t} \left(k\nabla^2 T + \eta \dot{W}^p + \dot{W}^{ve} + \dot{W}^{fric}\right) dt}{\rho c_p}. \tag{27}$$

Clearly, mass density and specific heat inversely affect heating. Since the thermal and mechanical processes are fully coupled and influence each other, this inverse relation is only a first-order effect. Specifically, changes in ρ and c_p also affect the dissipations in the above relation. To assess how the dissipations change as the two parameters are changed, the thermal forces due to viscoplasticity and friction that contribute to temperature change are also plotted in Fig. 15. It can be seen that the specific heat has little influence on the overall heat generation (Fig. 15(a)) which includes the main terms on the right hand side of Eq. (27); in contrast, binder density significantly changes the overall heat generation primarily by affecting frictional dissipation; PBX with lower binder mass density has more frictional dissipation, and vice versa (Fig. 15(b)). Fig. 15 also shows that the bulk viscoplastic dissipation (Fig. 15(c)) is not significantly affected by ρ or c_p. Fig. 16 outlines the spatial distribution of crack density in the loading direction (the spatial average in each strip perpendicular to the loading direction obtained by dividing the total crack length in that strip by the area of the strip, as discussed in Section 3.1, in mm/mm^2) by the types of fracture sites. Crack density in each subfigure represents extent of fracture in the location specified. Compared with fracture in the binder (Fig. 16(b)), fracture is more severe in the grains (Fig. 16(c)) and at the grain-binder boundaries (Fig. 16(d)). Furthermore, PBXs with low binder mass density have more cracks in the grains (Fig. 16(c)) and at the boundaries (Fig. 16(d)). Fig. 17 shows the spatial distribution of frictional dissipation by the same types of fracture sites as in Fig. 16. The frictional dissipation is approximately proportional to the crack density at each location. Both are localized in regions near the impact surface. As the distance from the impact surface increases, both decrease. The cracks in grains (Fig. 17(c)) and at grain-binder boundaries (Fig. 17(c)) account for most of the frictional heating. More importantly, the grain-binder interfacial heating is much more sensitive to binder properties (binder mass density in particular), with lower binder density resulting in significantly higher frictional dissipation at the boundaries (Fig. 17(d)). This explains the fact that

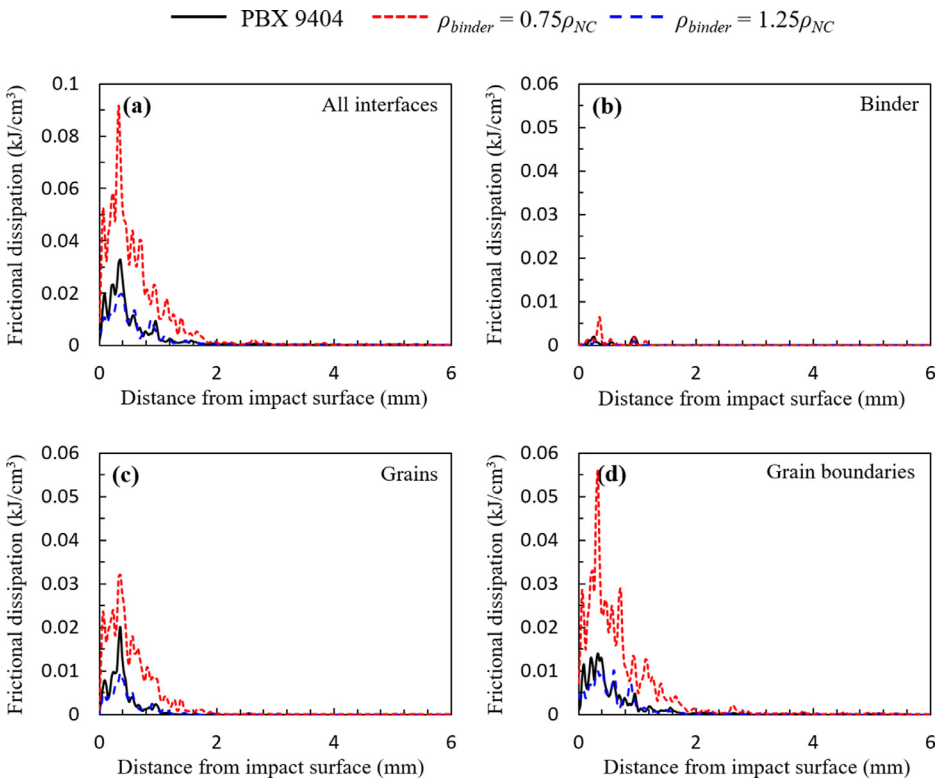

Fig. 17. Profiles of frictional dissipation per unit volume for PBX 9404 and variations of PBX 9404 with different binder mass density values: (a) at all interfaces, (b) in a binder, (c) in grains, and (d) at grain-binder boundaries. $U_p = 800$ m/s, $\tau = 120$ ns, and $\Delta t = 1.6$ μs.

the ignition threshold shows significantly stronger dependence on binder density (Fig. 14) than on binder specific heat and why binder is important in the first place.

4. Conclusion

In the design of new materials, it is important to establish and predict macroscopic, engineering measures of material performance as functions of microstructure. Predictive capabilities should allow exploration of material configurations not yet in existence, in addition to analysis of existing materials. In the process, it is also essential to capture stochastic variations in material behaviors arising from intrinsic microscopic heterogeneities. A computational approach for predicating the initiation thresholds of composite polymer-bonded explosives such as PBX 9404 has been developed. The prediction does not involve calibration or curve fitting with respect to experimental observations on initiation threshold, nor does it require prior information about the predicted behavior. Instead, the prediction is based on material microstructural attributes and fundamental constituent properties and uses multiphysics simulations that account for the underlying thermo-mechanical processes that determine the material behavior. While the approach is applicable to all loading conditions, pulse loading arising from planar impact involving thin flyers is considered in the analyses carried out, as that is a configuration that allows precise control of energy input to specimens in experiments. The simulations consider the configuration and conditions of actual experiments performed by Weingart et al. (1980), accounting for the thermo-mechanical shock response involving the elasto-viscoplasticity of HMX, visco-elasticity of nitrocellulose binder, fracture, post-fracture contact and friction along interfaces, pressure-dependence of the volumetric response, bulk inelastic heating and interfacial frictional heating, and heat conduction. The predicted initiation threshold of PBX 9404 is in good agreement with results from shock experiments reported in the literature.

The initiation thresholds obtained are analyzed and presented in the form of Walker–Wasley relation ($P^2\tau = C$) and the James relation ($\Pi_c/\Pi + E_c/E = 1$). The stochastic nature of the initiation behavior is analyzed and quantified using probability distribution functions, yielding explicit expressions for the ignition probability in terms of loading parameters. Important measures for the distribution functions for a given material are the standard deviations. The expressions can be used to evaluate ignition probabilities at any level of loading in any load parameter space of interest, although the particular spaces used in this study are the Walker–Wasley and James spaces.

The framework and analytical models presented in this study are not limited specifically to PBX 9404. This analysis can be performed on materials with other constituents. A parametric study shows that the mechanical and thermal properties

of the binder significantly affect the macroscopic ignition behavior of PBXs. Specifically, higher binder density and specific heat can reduce local temperature rise, and consequently, raise the ignition thresholds and lead to less sensitive EM design.

The analysis here also applies to materials with any combination of energetic particles and polymer binders, including systems with one constituent (e.g., pressed energetic particles), or systems with multiple constituents (e.g., energetic particles, a binder, and metallic fuel particles). In fact, systems with one type of pressed energetic particles have been studied (Kim et al., 2016), with the computationally predicted thresholds in a good agreement with experimental measurements. Three-constituent systems (aluminized PBX which has a binder, an energetic particle population, and an aluminum particle population) have been also studied (Kim et al., 2015), and again the computationally predicted ignition sensitivity shows the same trend as what is observed in experiments. It should be noted that microdefects and micropores have not been modelled, although the existence of those may lower the ignition threshold by increasing frictional heating on their contact surfaces. The consideration of defects and porosity is a topic of interest for a future publication. The capability developed and the insights gained can be used to design more advanced energetic materials and to analyze existing materials.

Acknowledgments

The authors gratefully acknowledge the support from the Air Force Office of Scientific Research (Dr. Martin Schmidt) through grants FA9550-15-1-0499 and FA9550-14-1-0201 and the Defense Threat Reduction Agency (DTRA) (Dr. Douglas Allen Dalton) through grants HDTRA1-15-1-0042 and HDTRA1-18-1-0004. Calculations are carried out on supercomputers at the ERDC and AFRL DSRCs of the U.S. DoD High Performance Computing Modernization Program.

References

Austin, R.A., Barton, N.R., Reaugh, J.E., Fried, L.E., 2015. Direct numerical simulation of shear localization and decomposition reactions in shock-loaded HMX crystal. J. Appl. Phys. 117, 185902.
Baer, M.R., 2002. Modeling heterogeneous energetic materials at the mesoscale. Thermochim. Acta 384, 351–367.
Barua, A., Zhou, M., 2011. A Lagrangian framework for analyzing microstructural level response of polymer-bonded explosives. Model. Simul. Mater. Sci. Eng. 19, 055001.
Barua, A., Kim, S., Horie, Y., Zhou, M., 2013a. Ignition criterion for heterogeneous energetic materials based on hotspot size-temperature threshold. J. Appl. Phys. 113, 064906.
Barua, A., Kim, S., Horie, Y., Zhou, M., 2013b. Prediction of probabilistic ignition behavior of polymer-bonded explosives from microstructural stochasticity. J. Appl. Phys. 113, 184907.
Barua, A., Kim, S., Horie, Y., Zhou, M., 2013c. Computational analysis of ignition in heterogeneous energetic materials. Mater. Sci. Forum 767, 13–21.
Bennett, J.G., Haberman, K.S., Johnson, J.N., Asay, B.W., 1998. A constitutive model for the non-shock ignition and mechanical response of high explosives. J. Mech. Phys. Solids 46, 2303–2322.
Benson, D.J., Conley, P., 1999. Eulerian finite-element simulations of experimentally acquired HMX microstructures. Model. Simul. Mater. Sci. Eng. 7, 333–354.
Chidester, S.K., Green, S.L., Lee, C., 1993. A Frictional Work Predictive Method for the Initiation of Solid High Explosives from Low-Pressure Impacts.. Lawrence Livermore National Lab., CA (United States).
Chidester, S.K., Tarver, C.M., Garza, R., 1998. Low amplitude impact testing and analysis of prestine and aged solid high explosives. In: Eleventh International Detonation Symposium. Snowmass, CO, p. 93.
Christiansen, D.E., Taylor, J.W., 1973. HE Sensitivity Study. Los Alamos Scientific Lab., Los Alamos. NM LA-5440-MS.
Dattelbaum, D.M., Stevens, L.L., 2008. Chapter 4 Equations of state of binders and related polymers. In: Peiris, S.M., Piermarini, G.J. (Eds.), Static Compression of Energetic Materials. Springer, Virginia, USA, pp. 127–202.
Dick, J.J., Hooks, D.E., Menikoff, R., Martinez, A.R., 2004. Elastic-plastic wave profiles in cyclotetramethylene tetranitramine crystals. J. Appl. Phys. 96, 374–379.
Frank-Kamenetskii, D.A., 1969. Diffusion and Heat Exchange in Chemical Kinetics.. Plenum Press, New York.
Gilbert, J., Chakravarthy, S., Gonthier, K.A., 2013. Computational analysis of hot-spot formation by quasi-steady deformation waves in porous explosive. J. Appl. Phys. 113.
Gittings, E.F., 1965. Initiation of a solid explosive by a short-duration shock. In: Proceedings of Fourth Symposium (International) on Detonation. Arlington, pp. 373–380.
Gonthier, K.A., 2003. Modeling and analysis of reactive compaction for granular energetic solids. Combust. Sci. Technol. 175, 1679–1709.
Green, L., Weston, A., Van Velkinburg, J., 1971. Mechanical and Frictional Behavior of Skid Test Hemispherical Billets. California University, Livermore Lawrence Livermore Lab.
Gresshoff, M., Hrousis, C.A., 2010. Probabilistic shock threshold criterion. 14th International Detonation Symposium. Coeur d'Alene, ID.
Gump, J.C., Peiris, S.M., 2005. Isothermal equations of state of beta octahydro-1,3,5,7-tetranitro-1,3,5,7-tetrazocine at high temperatures. J. Appl. Phys. 97, 053513.
Hardin, D.B., 2015. The Role of Viscoplasticity in the Deformation and Ignition Response of Polymer Bonded Explosives. Mechanical Engineering, Georgia Institute of Technology Doctor of Philosophy.
Hayes, D.B., 1976. 6th International Detonation Symposium. Coronado, CA, pp. 95–100.
Hodowany, J., Ravichandran, G., Rosakis, A.J., Rosakis, P., 2000. Partition of plastic work into heat and stored energy in metals. Exp. Mech. 40, 113–123.
Honodel, C.A., Humphrey, J.R., Weingart, R.C., Lee, R.S., Kramer, P., 1981. Shock initiation of TATB formulations. In: 7th International Detonation Symposium. Annapolis, MD, p. 325.
James, H.R., 1996. An extension to the critical energy criterion used to predict shock initiation thresholds. Propell. Explosiv. Pyrotech. 21, 8–13.
James, H.R., Lambourn, B.D., 2006. On the systematics of particle velocity histories in the shock-to-detonation transition regime. J. Appl. Phys. 100, 084906.
Kim, S., Barua, A., Horie, Y., Zhou, M., 2014. Ignition probability of polymer-bonded explosives accounting for multiple sources of material stochasticity. J. Appl. Phys. 115, 174902.
Kim, S., Horie, Y., Zhou, M., 2015. Ignition desensitization of PBX via aluminization. Metallurg. Mater. Trans. A 46, 4578–4586.
Kim, S., Miller, C., Horie, Y., Molek, C., Welle, E., Zhou, M., 2016. Computational prediction of probabilistic ignition threshold of pressed granular octahydro-1,3,5,7-tetranitro-1,2,3,5-tetrazocine (HMX) under shock loading. J. Appl. Phys. 120, 115902.
Landerville, A.C., Conroy, M.W., Budzevich, M.M., Lin, Y., White, C.T., Oleynik, I.I., 2010. Equations of state for energetic materials from density functional theory with van der Waals, thermal, and zero-point energy corrections. Appl. Phys. Lett. 97, 251908.
Levesque, G., Vitello, P., Howard, W.M., 2013. Hot-spot contributions in shocked high explosives from mesoscale ignition models. J. Appl. Phys. 113, 233513.
Liu, C., 2003. Specific Surface: A Missing Parameter in High-Explosive Modeling. Los Alamos National Laboratory (LANL), Los Alamos, NM (United States) LA-UR-14-20512.

Mas, E.M., Clements, B.E.. A viscoelastic model for PBX binders.
Mas, E.M., Clements, B.E., Blumenthal, B., Cady, C.M., Gray, G.T., Liu, C., 2002. A viscoelastic model for PBX binders. AIP Conf. Proc. 620, 661–664.
Mas, E.M., Clements, B.E., Ionita, A., Peterson, P., 2006. Finite element method calculations on statistically consistent microstructures of PBX 9501. AIP Conf. Proc. 845, 487–490.
Marsh, S.P., 1980. LASL Shock Hugoniot data. Los Alamos Series on Dynamic Material Properties. University of California, Berkeley, CA.
Menikoff, R., 2002. Compaction wave profiles in granular HMX. In: Shock Compression of Condensed Matter. Melville, pp. 979–982.
Miller, M.S., 1997. Thermophysical Properties of Six Solid Gun Propellants. Army Research Lab, Aberdeen Proving Ground. MD ARL-TR-1322.
Moore, D.S., McGrane, S.D., Funk, D.J., 2007. Ultrashort laser shock dynamics. In: Horie, Y. (Ed.), ShockWave Science and Technology Reference Library. Springer, Berlin. Heidelberg, pp. 47–104.
Mulford, R.N., Swift, D.C., 2002. Mesoscale modelling of shock initiation in HMX-based explosives. In: Shock Compression of Condensed Matter-2001, Pts 1 and 2, Proceedings, 620, pp. 415–418.
Rai, N.K., Udaykumar, H.S., 2015. Mesoscale simulation of reactive pressed energetic materials under shock loading. J. Appl. Phys. 118, 245905.
Rajic, M., Suceska, M., 2000. Influence of ageing on nitrocellulose thermal properties and hazard potential figures-of-merit. High Temperatures-High Pressures 32, 171–178.
Roth, J., 1970. Shock sensitivity and shock Hugoniots of high-density granular explosives. Fourth Symposium (International) on Detonation. White Oak.
Saw, C.K., 2002. Kinetics of HMX and phase transitions: effects of grain size at elevated temperature. In: Proceedings of the 12th International Detonation Symposium.
Shoemaker, R.L., Stark, J.A., Koshigoe, L.G., Taylor, R.E., 1985. Thermophysical properties of propellants. In: Ashworth, T., Smith, D.R. (Eds.). In: Thermal Conductivity, 18. Springer US, Boston, MA, pp. 199–211.
Solov'ev, V.S., 2000. Some specific features of shock-wave initiation of explosives. Combustion Explosion and Shock Waves 36, 734–744.
Springer, H.K., Tarver, C.M., Reaugh, J.E., May, C.M., 2014. Investigating short-pulse shock initiation in HMX-based explosives with reactive meso-scale simulations. J. Phys. Conf. Ser. 500, 052041.
Swift, D., Mulford, R., Winter, R., Taylor, P., Salisbury, D., Harris, E., et al., 2002. Mesoscale,modelling of reaction in HMX-based explosives. In: Twelfth International Detonation Symposium. San Diego, CA, p. 967.
Swift, D.C., Niemczura, J.G., Paisley, D.L., Johnson, R.P., Luo, S.N., Tierney, T.E., 2005. Laser-launched flyer plates for shock physics experiments. Rev. Sci. Instrum. 76.
Tarver, C.M., Chidester, S.K., Nichols, A.L., 1996. Critical conditions for impact- and shock-induced hot spots in solid explosives. J. Phys. Chem. 100, 5794–5799.
Trott, B., Jung, R., 1970. Effect of pulse duration on the impact sensitivity of solid explosives. In: Proceedings Fifth Symposium (International) on Detonation. Pasadena, CA, pp. 191–205.
Tucker, J., 2013. A Whole Life Assessment of Extruded Double Base Propellants. Department of Engineering and Applied Science, Cranfield University.
Vandersall, K.S., Tarver, C.M., Garcia, F., Chidester, S.K., 2010. On the low pressure shock initiation of octahydro-1,3,5,7-tetranitro-1,3,5,7-tetrazocine based plastic bonded explosives. J. Appl. Phys. 107, 094906.
Walker, F.E., Wasley, R.J., 1969. Critical energy for shock initiation of heterogeneous explosives. Explosivstoffe 17, 9–13.
Weingart, R.C., Jackson, R.K., Honodel, C.A., Lee, R.S., 1980. Shock initiation of PBX-9404 by electrically driven flyer plates. Propell. Explosiv. 5, 158–162.
Welle, E.J., Molek, C.D., Wixom, R.R., Samuels, P., 2014a. Microstructural effects on the ignition behavior of HMX. J. Phys. Conf. Ser. 500, 052049.
Welle, E.J., Molek, C.D., Wixom, R.R., Samuels, P., Langhals, J., 2014b. Microstructure effects on the initiation threshold behavior of HMX and PBXN-5. 15th International Detonation Symposium.
Wemhoff, A.P., Burnham, A.K., Nichols, A.L., Knap, J., 2007. Calibration methods for the extended prout-tompkins chemical kinetics model and derived cookoff parameters for RDX, HMX, LX-10 and PBXN-109. In: ASME-JSME Thermal Engineering Summer Heat Transfer Conference. Vancouver, British Columbia, CANADA, pp. 625–632.
Wu, Y.Q., Huang, F.L., 2009. A micromechanical model for predicting combined damage of particles and interface debonding in PBX explosives. Mech. Mater. 41, 27–47.
Yoo, C.S., Cynn, H., 1999. Equation of state, phase transition, decomposition of beta-HMX (octahydro-1,3,5,7-tetranitro-1,3,5,7-tetrazocine) at high pressures. J. Chem. Phys. 111, 10229–10235.
Zhai, J., Tomar, V., Zhou, M., 2004. Micromechanical simulation of dynamic fracture using the cohesive finite element method. J. Eng. Mater. Technol.-Trans. ASME 126, 179–191.
Zhou, M., Needleman, A., Clifton, R.J., 1994. Finite-element simulations of shear localization in plate impact. J. Mech. Phys. Solids 42, 423–458.